



23 Seawater is utilised as the phase-change material and it is pre-desalinated in the energy  
 24 storage subcycle. A mathematical model of the system is established and experimental  
 25 investigation is conducted. Furthermore, the theoretical and experimental performances  
 26 are compared, and an economic analysis of seawater desalination is performed to  
 27 evaluate its economy. The results show that the total refrigeration output of the system  
 28 ranges from 6.1 kW to 9.9 kW, and the system COP (Coefficient of Performance) can  
 29 reach 16% under the experimental operating conditions. Additionally, the salinity of  
 30 pre-desalinated seawater can be reduced to below 10 ppt. Moreover, the cost of RO  
 31 (Reverse Osmosis) seawater desalination can be reduced by 26% through the pre-  
 32 desalination process of seawater.

33

34 **Keywords:** Marine diesel engine; Exhaust gas heat recovery; Absorption refrigeration;  
 35 Ammonia–water; Seawater freezing desalination

36

37

<b>Nomenclature</b>	
<b>Symbols</b>	
<i>B</i>	ratio of washing water to sea ice
<i>F</i>	cost, yuan
<i>G</i>	reflux ratio
<i>J</i>	icing rate
<i>P</i>	pressure, MPa
<i>Q</i>	heat load, kW
<i>T</i>	temperature, °C
<i>U</i>	circulation ratio
<i>X</i>	solution concentration, kg/kg
<i>Z</i>	refrigeration ratio between evaporator I and II
<i>c<sub>p</sub></i>	seawater specific heat, kJ/(kg °C)
<i>h</i>	specific enthalpy, kJ/kg
<i>m</i>	mass flow rate, kg/s
<i>n</i>	desalinization ratio

<i>q</i>	specific heat load, kJ/kg
<i>s</i>	seawater salinity, ppt
<b>Greek Symbols</b>	
$\alpha$	rate of pre-desalinated water output, %
$\Delta$	temperature difference, °C
<b>Subscripts</b>	
<i>R</i>	reflux condenser
<i>a</i>	absorber
<i>c</i>	condenser
<i>e</i>	evaporator
<i>g</i>	generator
<i>i=1,2,3...</i>	state points
<i>r</i>	rich solution
<i>w</i>	weak solution
<i>ps</i>	pre-desalinated seawater
<i>sh</i>	solution heat exchanger
<i>sw</i>	seawater
<i>ww</i>	washing water
<i>con</i>	condensation
<i>ice</i>	sea ice
<i>mem</i>	RO membrane
<i>ref</i>	refrigerant
<i>elec</i>	electricity
<b>Acronyms</b>	
<i>ABS</i>	absorber
<i>AM-TANK</i>	ammonia tank
<i>CAP</i>	capillary
<i>CON</i>	condenser
<i>CO-STO</i>	cold storage
<i>DEP</i>	dephlegmator
<i>EVAP</i>	evaporator
<i>GEN</i>	generator
<i>H-EXCH</i>	solution heat exchanger
<i>NOZ</i>	nozzle
<i>REF-CON</i>	reflux condenser
<i>RO-D</i>	RO device
<i>TH-TANK</i>	thawing tank
<i>VIB-SEP</i>	vibrant separator
<i>fre-water</i>	fresh water
<i>gas-in</i>	exhaust gas inlet
<i>gas-out</i>	exhaust gas outlet

<i>pre-water</i>	pre-desalinated seawater
<i>was-water</i>	washing water
<i>water-in</i>	cooling water inlet
<i>w-out</i>	cooling water outlet

38 **1. Introduction**

39 Marine diesel engines have been widely used as the primary power suppliers for  
40 fishing and merchant ships[1]. When a marine diesel engine operates in the zone of  
41 good efficiency, only 30–45% of the energy obtained by fuel combustion can be  
42 transferred into shaft power output[2-4], while approximately one third of the energy is  
43 wasted along with the exhaust gases[5]. Consequently, the waste heat recovery of  
44 engine exhaust gas is important for improving the fuel efficiency and achieving the goal  
45 of energy conservation in marine diesel engines[6, 7]. In addition, it aids in  
46 environmental protection by reducing carbon dioxide emissions[8].

47 Among the several exhaust gas heat recovery technologies available, absorption  
48 refrigeration cycle technology has proven to be the most effective as it converts exhaust  
49 heat energy into refrigeration output[9, 10]. Generally, the absorption refrigeration  
50 cycle is categorised into two types: the lithium-bromide-based absorption refrigeration  
51 cycle[11] and the ammonia–water-based absorption refrigeration cycle[12]. Owing to  
52 the crystallisation in the operating fluid, the refrigeration temperature of lithium-  
53 bromide-based absorption refrigeration cycle remains above zero[13-15], while the  
54 refrigeration temperature of an ammonia–water-based cycle can reach approximately  
55 –30 °C[16-18] and can be used for cryogenic refrigeration[19]. Therefore, the  
56 ammonia–water-based cycle is more competitive for marine cryogenic refrigeration,  
57 particularly for fishing ship refrigeration.

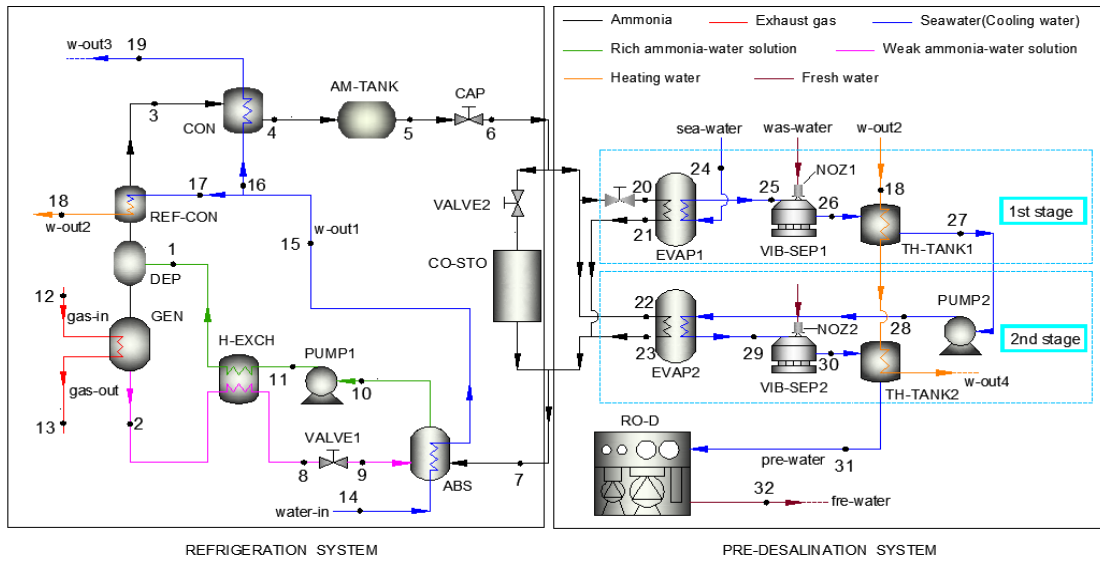
58        However, the disadvantage of ammonia–water-based absorption refrigeration cycle  
59        that is driven by exhaust gas is obvious: after the temperature of cold storage reaches  
60        the predetermined refrigerating temperature, the refrigeration demand of cold storage  
61        declines to a low level. While the electric compression refrigeration system can adopt  
62        an intermittent operation strategy to adapt to the fluctuation of the refrigeration  
63        demand[20], the absorption refrigeration system is more inflexible as it is driven by the  
64        exhaust gas and its cooling capacity can become redundant. Therefore, it is important  
65        to balance the excessive refrigerating output.

66        To solve this problem, ice thermal storage technology can be considered. Ice  
67        thermal storage technology is a type of phase-change energy storage technology[21,  
68        22]. By storing the redundant cooling capacity in the form of an ice slurry[23, 24], the  
69        refrigerating output can be fully utilised. If seawater is used as the phase-change  
70        material, it can be pre-desalinated owing to the freezing desalination phenomenon.  
71        Freezing desalination is based on the fact that salt is separated during the formation of  
72        ice crystals. Fresh water can then be produced by harvesting and melting the ice  
73        crystals[25-27]. The technology of freezing desalination was first applied in food  
74        concentration. In 1961, Shapiro applied the freezing concentration method to an  
75        experiment that concentrated organic compounds[28]. Currently, using the freezing  
76        method for seawater desalination has attracted wide attention. Anouar Rich et al. [29]  
77        improved the purity of sea ice using partial melting to drain out trapped brine pockets.  
78        Cong-shuang Luo et al. [30] employed unidirectional freezing to create layered ice and  
79        subsequently improved the quality of ice through crushing and centrifugation. In

80 general, seawater freezing desalination is effective in terms of energy utilisation, and  
81 has many advantages in comparison to other conventional technologies[31]. After the  
82 process of freezing desalination, the salinity of seawater will be significantly reduced.  
83 This is important in the application of the absorption refrigeration system on board a  
84 ship. With a lower level of salinity in seawater, the operation pressure of the RO device  
85 can significantly be decreased. On the one hand, the service life of the RO membrane  
86 is extended; while the operation power of the high-pressure pump is decreased. The  
87 factors above can effectively reduce the cost of RO seawater desalination.

88       Herein, an absorption refrigeration and freezing pre-desalination system for marine  
89 engine exhaust gas heat recovery is proposed. In this system, waste heat from the  
90 internal combustion engine exhaust gas is used to drive the ammonia-absorption  
91 refrigeration cycle. When the cooling capacity is provided, the partial cooling capacity  
92 is used for seawater pre-desalination according to the seawater freezing desalination  
93 principle, and the remaining cooling capacity is used to conserve food in cold storage.  
94 This system avoids the waste of exhaust gas energy through incessant seawater pre-  
95 desalination, which can be deemed as a disguised energy-storage technology. In  
96 addition, the mathematical model of the absorption refrigeration and pre-desalination  
97 system for marine engine exhaust gas heat recovery is established, and the performance  
98 of the system is theoretically analysed. Furthermore, an experimental platform is built  
99 and experimental tests are conducted. The theoretical and experimental results are  
100 compared, and an economic analysis of seawater desalination is performed to evaluate  
101 its economy.

102 **2. System description**

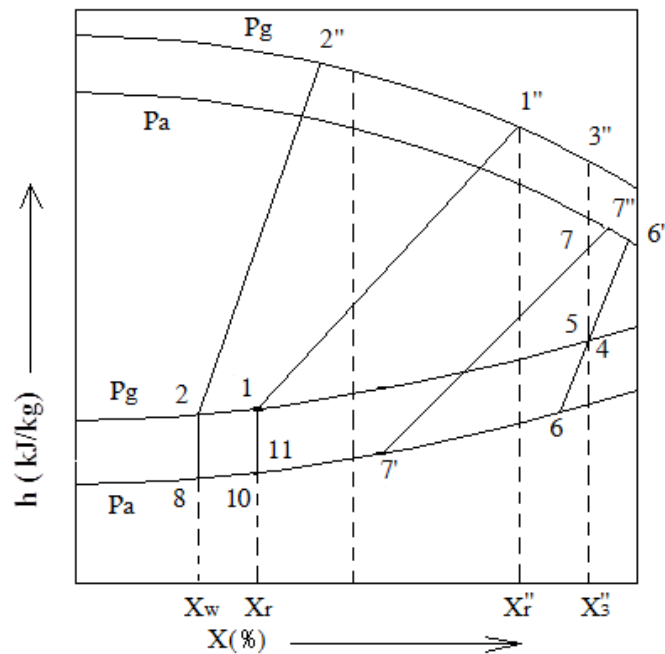


103

104 Fig.1 Schematic of the absorption refrigeration and two-stage freezing-assisted

105 desalination system (the abbreviations in the figure can be found in the nomenclature

106 section)



107

108 Fig.2 h-X diagram of the refrigeration cycle

109 Figure 1 shows a schematic of the combined system and Fig. 2 shows the h-X

110 diagram of the refrigeration cycle. The proposed system consists of the following  
111 primary components:

- 112 • A generator
- 113 • A dephlegmator
- 114 • A reflux condenser
- 115 • A condenser
- 116 • An ammonia tank
- 117 • An absorber
- 118 • A heat exchanger
- 119 • A capillary
- 120 • A cold storage
- 121 • A solution pump
- 122 • Two evaporators
- 123 • Two vibrant separators
- 124 • Two thawing tanks
- 125 • Two nozzles
- 126 • Three valves

127 The absorption refrigeration and two-stage freezing-assisted desalination system  
128 contains two subsystems: refrigeration subsystem and pre-desalinated subsystem. The  
129 refrigeration subsystem is a single-stage ammonia–water absorption refrigeration  
130 system, which is driven by marine engine exhaust gas heat. The pre-desalinated  
131 subsystem is a two-stage seawater freezing-assisted desalination system. In the pre-



132 desalinated subsystem, seawater is used as the phase-change energy storage material  
133 and it is pre-desalinated owing to the freezing desalination phenomenon.

134 The detailed process description of the combined system is as follows:

135 In the refrigeration system, the high-temperature flue gas produced by the marine  
136 diesel engine is used as a heating source. In the generator, a high-temperature and high-  
137 pressure ammonia–water mixture is generated and subsequently, successively passed  
138 through the dephlegmator and reflux condenser. The high-temperature ammonia vapour  
139 is separated from the ammonia–water mixture, before entering the condenser and the  
140 capillary to further reduce the temperature. In this process, the ammonia vapour  
141 becomes a low-temperature ammonia liquid. Next, the ammonia liquid flows into two  
142 branches to produce refrigeration: the cold storage branch and the freezing desalination  
143 branch. After evaporation to the two branches above, the ammonia vapour is mixed and  
144 flows into the absorber. Meanwhile, the separated weak ammonia–water solution is  
145 cooled down in the solution heat exchanger, and it is subsequently passed through the  
146 throttle valve to reduce pressure, before flowing into the absorber to produce a rich  
147 solution. The cooling water is used to eliminate the heat generated in the absorption  
148 process and to remove the heat of condensation in the condenser and reflux condenser.  
149 Finally, the rich solution at a relatively low temperature and pressure is pumped into  
150 the generator after being heated in the solution heat exchanger.

151 In the pre-desalination system, a two-stage freezing-assisted desalination approach  
152 is adopted. First, a part of the ammonia liquid is evaporated in evaporator I to produce  
153 first-level refrigeration. The initial seawater is turned into an ice water mixture after

154 acquiring the first-level refrigeration. The ice water mixture enters vibrant separator I  
155 through the outlet of evaporator I to separate. Simultaneously, fresh water from the  
156 nozzle washes the sea ice to reduce its salinity. This part of the fresh water is also  
157 considered in the final economic analysis. Subsequently, the sea ice enters thawing tank  
158 I to exchange heat with the relatively high-temperature cooling water from the reflux  
159 condenser outlet. After thawing, the seawater with an initial reduction in salinity is  
160 pumped into evaporator II to acquire second-level refrigeration. Meanwhile, the  
161 remaining ammonia liquid evaporates completely. The ice water mixture formed in this  
162 process enters vibrant separator II and thawing tank II successively to repeat the steps  
163 above, further reducing the salinity of the pre-desalinated seawater. Finally, the  
164 ammonia liquid in the desalination branch evaporates completely. The ammonia vapour  
165 from the desalination branch, along with the ammonia vapour from the cold storage  
166 branch, flow into the absorber together.

### 167 **3. Thermodynamic analysis of the combined system**

168 A thermodynamic analysis was conducted to assess the performance of the  
169 combined refrigeration and pre-desalination system. A mathematical model was  
170 established, where a program was developed to solve the equations.

#### 171 **3.1. Basic assumptions**

172 The following assumptions were used in the system modelling:

- 173 (1) Each component of this combined system is in a steady state.

- 174 (2) The heat losses in the system are negligible.
- 175 (3) The fluid expansion in the throttling valve is considered isenthalpic.
- 176 (4) The ammonia–water solution/vapour at the output of both the absorber and  
177 reflux condenser are saturated.

### 178 3.2. Mathematical model

179 The mathematical model for this combined system was established based on the  
180 first law of thermodynamics, and an energy analysis was conducted to evaluate the  
181 theoretical performance of this combined system.

182 The mass balance equations in the system are given as follows:

$$183 (\sum m_i)_{in} = (\sum m_i)_{out}; \quad (1)$$

$$184 (\sum X_i \cdot m_i)_{in} = (\sum X_i \cdot m_i)_{out}. \quad (2)$$

185 The energy balance equations for the system are given as follows:

186 The reflux ratio is defined as

$$187 G = m_2/m_3. \quad (3)$$

188 The degassing range is defined as

$$189 \Delta X = X_r - X_w. \quad (4)$$

190 The circulation ratio is defined as

$$191 U = (X_3 - X_w)/(X_r - X_w). \quad (5)$$

192 The unit heat exchange and total heat exchange of the reflux condenser are

$$193 q_R = h_1'' - h_3 + G(h_1'' - h_1); \quad (6)$$

$$194 Q_R = m_3 \cdot q_R, \quad (7)$$

195 where  $h_1''$  is the specific enthalpy of the gas phase in equilibrium with the  
196 ammonia–water solution at point 1.

197 The unit heat exchange and total heat exchange of the generator are

$$198 \quad q_g = h_3 - h_2 + U(h_2 - h_1) + q_R; \quad (8)$$

$$199 \quad Q_g = m_3 \cdot q_g. \quad (9)$$

200 The unit heat exchange and total heat exchange of the condenser are

$$201 \quad q_c = h_3 - h_4; \quad (10)$$

$$202 \quad Q_c = m_3 \cdot q_c. \quad (11)$$

203 The unit heat exchange and total heat exchange of the absorber are

$$204 \quad q_a = h_7 - h_9 + U(h_9 - h_{10}); \quad (12)$$

$$205 \quad Q_a = m_3 \cdot q_a. \quad (13)$$

206 The unit refrigerating capacity and total refrigerating capacity are

$$207 \quad q_e = h_7 - h_5; \quad (14)$$

$$208 \quad Q_e = m_3 \cdot q_e. \quad (15)$$

209 The unit heat exchange and total heat exchange of the solution heat exchanger are

$$210 \quad q_{sh} = (U - 1)(h_2 - h_8); \quad (16)$$

$$211 \quad Q_{sh} = m_3 \cdot q_{sh}. \quad (17)$$

212 The system coefficient of performance (COP) is

$$213 \quad \text{COP} = Q_e / Q_g. \quad (18)$$

214 The energy balance equation for the system is

$$215 \quad Q_e + Q_g = Q_R + Q_c + Q_a. \quad (19)$$

216 The analysis for the seawater side of the desalination branch is given as follows:

217 Assuming that cold consumption is not considered,  $Q_{ed}$  is the total refrigeration  
 218 of the desalination branch. To distribute the total refrigeration to evaporators I and II  
 219 according to the refrigeration ratio  $Z$ ,

220 the refrigeration of evaporator I is

$$221 \quad Q_1 = \frac{Z}{Z+1} Q_{ed}. \quad (20)$$

222 The refrigeration of evaporator II is

$$223 \quad Q_2 = \frac{1}{Z+1} Q_{ed}. \quad (21)$$

224 For evaporator I:  $T_{sw1}$  is the seawater inlet temperature;  $T_{sw2}$  is the outlet  
 225 temperature;  $J_1$  is the icing rate;  $B_1$  is the ratio of washing water to sea ice; and  $q_{con}$   
 226 is the unit condensation heat of seawater. The mass flow rate of the seawater to be  
 227 desalinated  $m_{sw1}$  can be calculated according to the refrigeration.

$$228 \quad Q_1 = c_p m_{sw1} (T_{sw1} - T_{sw2}) + m_{ice1} \cdot q_{con} \quad (22)$$

$$229 \quad m_{ice1} = J_1 \cdot m_{sw1} \quad (23)$$

230 The mass flow rate of the seawater entering evaporator I  $m_{sw1}$  can be acquired  
 231 according to equation (22) and equation (23).

232 The mass flow rate of the seawater entering evaporator II is

$$233 \quad m_{sw2} = m_{ice1}. \quad (24)$$

234 The mass flow rate of the washing water consumed by the first desalination  
 235 process is

$$236 \quad m_{ww1} = B_1 \cdot m_{ice1}. \quad (25)$$

237 The initial salinity of the seawater is defined as  $s_1$ . After the first desalination  
 238 process, the salinity of the seawater is defined as  $s_2$ , and the desalination ratio is

239 
$$n_1 = \frac{s_1 - s_2}{s_1} \times 100\%. \quad (26)$$

240 For evaporator II:  $T_{sw3}$  is the seawater inlet temperature;  $T_{sw4}$  is the outlet  
 241 temperature;  $J_2$  is the icing rate; and  $B_2$  is the ratio of washing water to sea ice. The  
 242 refrigerating capacity of evaporator II  $Q_{sw2}$  can be acquired according to the  
 243 calculation results above.

244 
$$Q_{sw2} = c_p m_{sw2} (T_{sw3} - T_{sw4}) + m_{ice2} \cdot q_{con} \quad (27)$$

245 
$$m_{ice2} = J_2 \cdot m_{sw2} \quad (28)$$

246  $Q_{sw2}$  can be compared with  $Q_2$ . If  $Q_{sw2} \leq Q_2$ , the calculation results are  
 247 reasonable; if  $Q_{sw2} > Q_2$ , the mass flow rate  $m_{sw1}$  of the seawater before entering  
 248 evaporator I should gradually be reduced, and subsequently the calculation steps above  
 249 should be repeated to obtain the new values of  $Q_{sw1}$  and  $Q_{sw2}$ .  $Q_{sw1}$  and  $Q_{sw2}$  are  
 250 the ultimate refrigerating capacities of evaporators I and II, respectively.

251 Finally, the mass flow rate of the pre-desalinated seawater with low salinity is

252 
$$m_{ps} = m_{ice2}. \quad (29)$$

253 The salinity of the seawater that enters evaporator II is  $s_2$ . After the second  
 254 desalination process, the salinity of the seawater is reduced to  $s_3$ , and the desalination  
 255 ratio is

256 
$$n_2 = \frac{s_2 - s_3}{s_2} \times 100\%. \quad (30)$$

257 After the complete desalination process, the total desalination ratio is

258 
$$n = \frac{s_1 - s_3}{s_1} \times 100\%. \quad (31)$$

259 The output ratio of the pre-desalinated seawater with low salinity is

260 
$$\alpha = \frac{m_{ps}}{m_{sw1}} \times 100\%. \quad (32)$$

261 The icing rates  $J_1$  and  $J_2$ , and the salinities  $s_2$  and  $s_3$  mentioned above are  
262 based on the following substep of the desalination experiment.

263 The analysis for the refrigerant side of the desalination branch is given as follows:

264 The total mass flow rate of the refrigerant in the desalination branch is defined as

$$265 \quad m_{ref} = m_{ref1} + m_{ref2}. \quad (33)$$

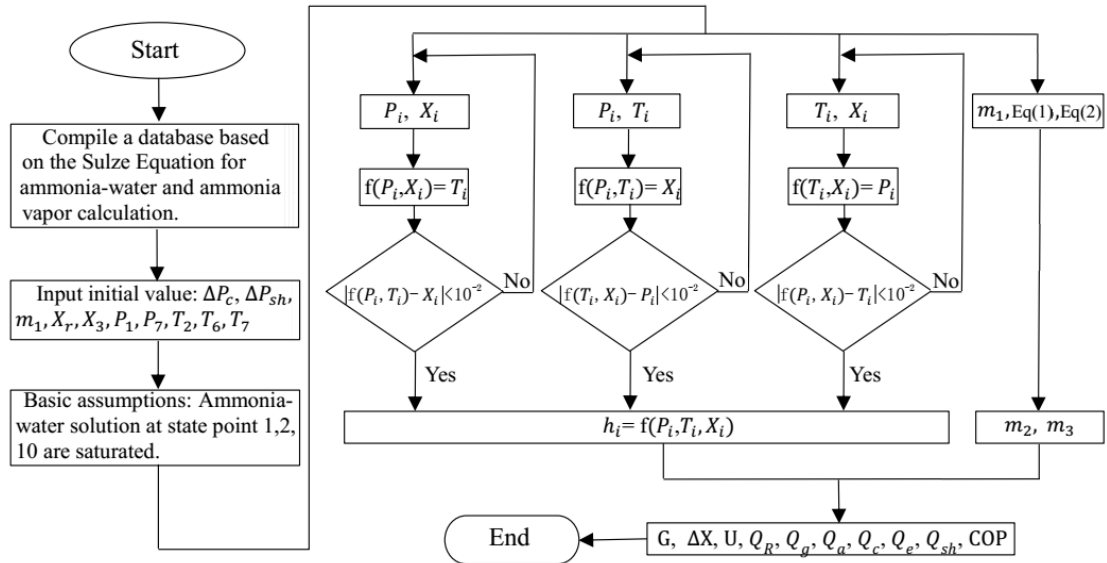
266 Assuming that the temperature of the refrigerant before entering the evaporator is  
267  $T_{ref1}$ , the enthalpy of the saturated ammonia liquid is  $h_{ref1}$ . After evaporation, the  
268 temperature of the ammonia vapour increases to  $T_{ref2}$ , and the enthalpy of the  
269 saturated ammonia vapour is  $h_{ref2}$ . According to the above analysis, the refrigerating  
270 capacities of evaporators I and II are  $Q_{s1}$  and  $Q_{s2}$ , respectively. Subsequently, the  
271 mass flow rates of the evaporated refrigerant for evaporators I and II, respectively, are

$$272 \quad m_{ref1} = \frac{Q_{s1}}{h_{ref2} - h_{ref1}}; \quad (34)$$

$$273 \quad m_{ref2} = \frac{Q_{s2}}{h_{ref2} - h_{ref1}}. \quad (35)$$

### 274 3.3. Solution procedure

275 A program was developed to analyse the system performance; Fig. 3 shows the  
276 calculation strategy for the refrigeration system. In this program, a database was  
277 compiled based on the Sulze equation[32] to calculate the thermodynamic variables of  
278 the ammonia–water and ammonia vapour. Table 1 shows the initial parameters for the  
279 simulation.



280

281

Fig. 3 Solution procedure for the refrigeration system

282 **Table 1** Initial parameters for simulation

Diesel engine specification	200 kW	Generation temperature	150 °C
Evaporation temperature	-18 °C	Cooling water temperature	25 °C
Rich solution concentration	0.28 kg/kg	Rich solution mass flow rate	40 g/s
Generation pressure	1.0 MPa	Absorption pressure	0.1 MPa
Pressure difference between generator and condenser	0.1 MPa	Pressure drop of solution heat exchanger	0.2 MPa

283 **3.4. Results and performance**

284 To obtain the details of the thermodynamic performance of the refrigeration system,

285 a simulation under a typical operating condition was performed. Table 2 shows the

286 simulation results of each state point in the refrigeration system at a typical operating

287 condition. In addition, the performance of the refrigeration system with this typical

288 operating condition is shown in Table 3.

289 **Table 2** Results of simulation at typical operating condition

State	X (kg/kg)	P (MPa)	T (°C)	H (kJ/kg)	M (g/s)
1	0.28	1	104	350	40
2	0.12	1	150	570	32.7
3	1.00	1	55	1792	7.3



4	1.00	1.1	30	639	7.3
5	1.00	1.1	30	639	7.3
6	1.00	0.1	-18	418	7.3
7	1.00	0.1	-15	1743	7.3
8	0.12	0.8	80	250	32.7
9	0.12	0.1	80	250	32.7
10	0.28	0.1	32	25	40
11	0.28	1.2	32	88	40

290

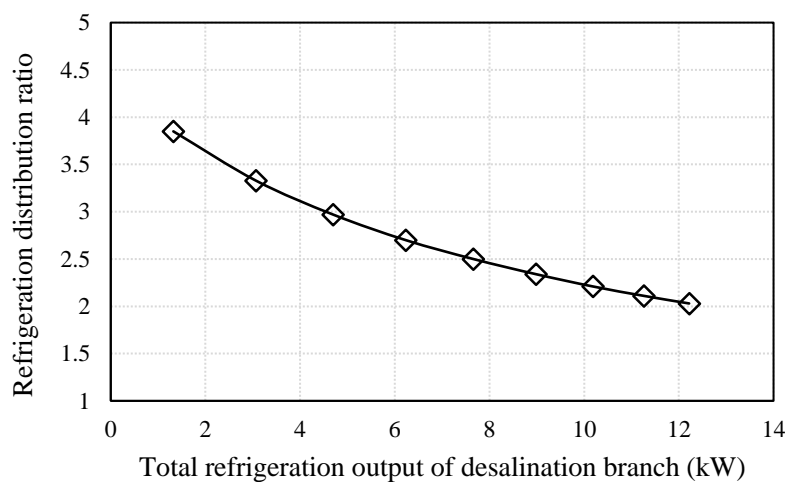
291 **Table 3** Performance of the refrigeration system

Reflux ratio	4.5
Degassing range (kg/kg)	0.16
Circulation ratio	5.5
Dephlegmator heat output (kW)	52.7
Generator heat input (kW)	70.5
Condenser heat output (kW)	8.4
Absorber heat output (kW)	19.9
Refrigeration output (kW)	8.1
COP (%)	11.5

292 The relationship between the total refrigerating capacity of the desalination branch

293  $Q_{ed}$  and the refrigeration ratio  $Z$  of evaporators I and II is shown in Fig. 4. The curve

294 in Fig. 4 is obtained from a variable-condition analysis by a further solution program.



295

296 Fig.4 Relationship between the total refrigeration capacity in desalination branch

297

and the refrigeration distribution ratio

298 **4. Experimental analysis of the combined system**

299 An experimental analysis of the combined system was performed, including an  
 300 uncertainty analysis of the experimental instruments, and analyses of the experimental  
 301 plan and results.

302 **4.1. Uncertainty analysis**

303 A set of instruments were mounted on each component. The instruments consist of  
 304 a thermocouple, pressure gauge, flowmeter, and flue gas analyser. The detailed  
 305 parameters of the instruments are listed in Table 4.

306 **Table 4** Parameters of instruments

K-type thermocouple	-40 to 1200 °C, ±0.5%
Pressure gauge	0–1.5 MPa, ±0.5%
Flowmeter for liquid ammonia	10–100 L/h, ±1.0%
Flue gas analyser	O <sub>2</sub> , CO <sub>2</sub> , N <sub>2</sub> , ±1.0%
Flowmeter for water	0.10–10 m <sup>3</sup> /h, ±1.5%
Flowmeter for exhaust gas	0–120 m/s, ±1.0%

307 The uncertainty analysis is based on the theory of error propagation and the root-  
 308 sum-square method to combine the errors, and the equations are listed as follows:

309 
$$\frac{\mu_{COP}}{COP} = \sqrt{\left(\frac{\mu_{Q_e}}{Q_e}\right)^2 + \left(\frac{\mu_{Q_g}}{Q_g}\right)^2}$$

310 
$$\frac{\mu_{Q_e}}{Q_e} = \sqrt{\left(\frac{\mu_{m_3}}{m_3}\right)^2 + \left(\frac{\mu_{h_5}}{h_5}\right)^2 + \left(\frac{\mu_{h_7}}{h_7}\right)^2}$$

311 
$$\frac{\mu_{Q_g}}{Q_g} = \sqrt{\left(\frac{\mu_{m_3}}{m_3}\right)^2 + \left(\frac{\mu_{h_1}}{h_1}\right)^2 + \left(\frac{\mu_{h_2}}{h_2}\right)^2 + \left(\frac{\mu_{h_3}}{h_3}\right)^2 + \left(\frac{\mu_U}{U}\right)^2 + \left(\frac{\mu_{q_R}}{q_R}\right)^2}$$

312 
$$\frac{\mu_{Q_R}}{Q_R} = \sqrt{\left(\frac{\mu_{m_3}}{m_3}\right)^2 + \left(\frac{\mu_{h_1}}{h_1}\right)^2 + \left(\frac{\mu_{h_3}}{h_3}\right)^2 + \left(\frac{\mu_G}{G}\right)^2}$$

313 
$$\frac{\mu_{Q_a}}{Q_a} = \sqrt{\left(\frac{\mu_{m_3}}{m_3}\right)^2 + \left(\frac{\mu_{h_7}}{h_7}\right)^2 + \left(\frac{\mu_{h_9}}{h_9}\right)^2 + \left(\frac{\mu_{h_{10}}}{h_{10}}\right)^2 + \left(\frac{\mu_U}{U}\right)^2}$$

314 
$$\frac{\mu_{Q_c}}{Q_c} = \sqrt{\left(\frac{\mu_{m_3}}{m_3}\right)^2 + \left(\frac{\mu_{h_3}}{h_3}\right)^2 + \left(\frac{\mu_{h_4}}{h_4}\right)^2}$$

$$\frac{\mu_G}{G} = \sqrt{\left(\frac{\mu_{m_2}}{m_2}\right)^2 + \left(\frac{\mu_{m_3}}{m_3}\right)^2}$$

$$\frac{\mu_U}{U} = \sqrt{\left(\frac{\mu_{X_3}}{X_3}\right)^2 + \left(\frac{\mu_{X_r}}{X_r}\right)^2 + \left(\frac{\mu_{X_w}}{X_w}\right)^2}$$

$$\mu_X = \sqrt{(X(T + \mu_T, P) - X(T, P))^2 + (X(T, P + \mu_P) - X(T, P))^2}$$

$$\mu_h = \sqrt{(h(T + \mu_T, P, X) - h(T, P, X))^2 + (h(T, P + \mu_P, X) - h(T, P, X))^2 + (h(T, P, X + \mu_X) - h(T, P, X))^2}$$

The resulting uncertainty in the COP is 3.8%. The uncertainty in the refrigerating capacity is 1.7%.

## 4.2. Experimental plan

The experimental plan includes the general system experimental plan and pre-desalination system experimental plan.

### 4.2.1. Experimental plan for combined system

The experimental platform for this combined system was constructed. A certain proportion of water and pure ammonia vapour were injected into the system, and the concentration of the formed rich solution was 0.28 kg/kg. Compared to the concentration of rich ammonia-water solution in traditional absorption refrigeration cycles, the concentration of 0.28 kg/kg is relatively low. The benefit of a low concentration is that it can reduce the pressure of the whole system. The temperature of the flue gas from the diesel engine was increased from 250°C to 350 °C to test the performance of the combined system.

The variations in the primary parameters with the increase in the generation temperature were recorded and analysed, including the generator heat input, condenser

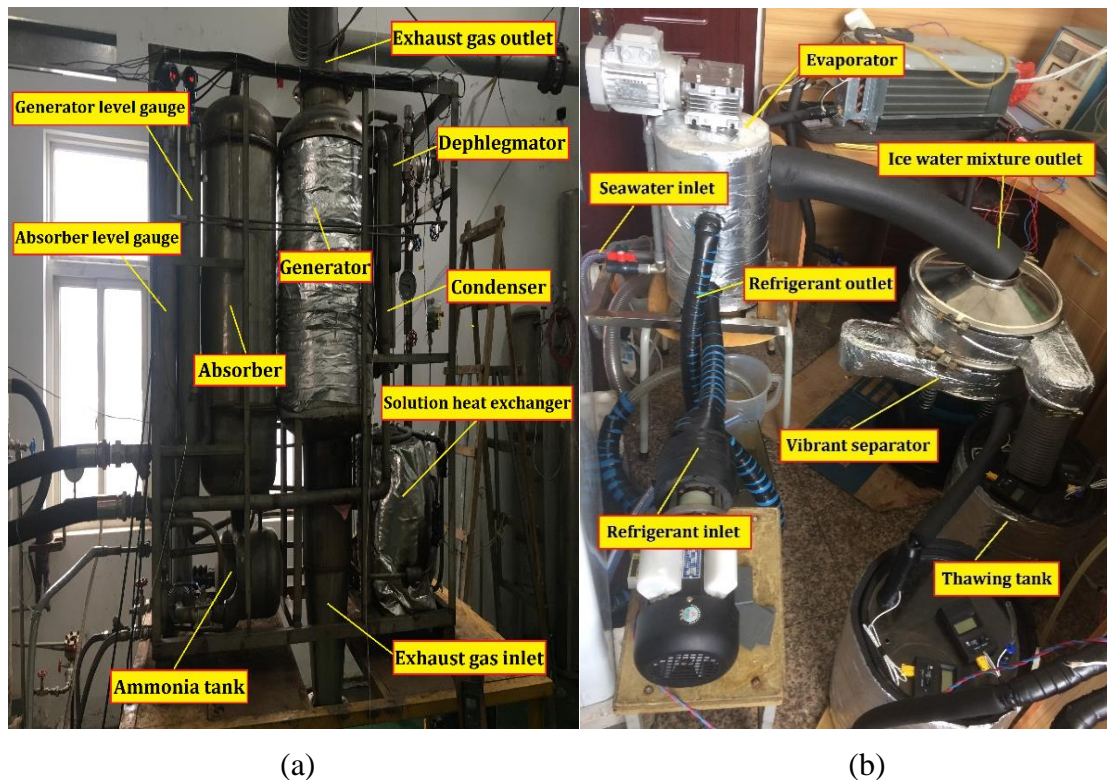
335 heat output, absorber heat output, refrigeration output, total ammonia production,  
336 ammonia flux in desalination branch, pre-desalinated seawater production, and pre-  
337 desalinated seawater salinity. In a stable operation, the ammonia flux of the desalination  
338 branch is maintained by controlling the valve. Therefore, the refrigeration output of the  
339 desalination branch and the production of pre-desalinated seawater can also be  
340 maintained.

341 The exhaust gas heat input for the combined system was calculated based on the  
342 components and the temperature at the exhaust gas inlet and outlet. The volume fraction  
343 of the primary components in the exhaust gas was measured by the flue gas analyser.  
344 Because  $N_2$ ,  $O_2$ ,  $CO_2$ , and  $H_2O$  constitute approximately 99.7% of the volume in the  
345 exhaust gas, the enthalpy of the exhaust gas can be obtained.

#### 346 **4.2.2. Experimental plan for pre-desalination**

347 Multiple repeated experiments were performed to test the performance of the pre-  
348 desalination system, and each experiment was divided into two stages. In the first stage,  
349 the initial seawater flow was 100 L/h. Under this seawater flow condition, the ammonia  
350 liquid flow at the inlet of the evaporator was adjusted to change the cooling capacity. If  
351 the cooling capacity is large, it increases the amount of sea ice, but the sea ice can easily  
352 form ice cubes, thus increasing the sea ice salinity. If the cooling capacity is small, the  
353 fluidity of the sea ice can be improved and the salinity can be reduced, but the amount  
354 of sea ice produced is little to none. Therefore, experiments are carried out to obtain the  
355 cooling capacity that is best suited for seawater crystallisation. The most suitable

356 standard is more amounts of ice and low salinity. According to the flow and salinity of  
357 the sea ice obtained after the evaporator in the first stage, the flow and salinity of the  
358 seawater that will enter the evaporator in the second stage was adjusted. Low-salinity  
359 seawater is composed of sea salt and fresh water. Subsequently, the ammonia liquid  
360 flow at the inlet of the evaporator was adjusted again to obtain the most suitable cooling  
361 capacity in the second stage. After the two-stage freezing-assisted pre-desalination  
362 process, the flow and salinity of the pre-desalinated sea ice was obtained.



365 Fig.5 Photographs of the experimental platform: (a) Refrigeration system;

366 (b) Desalination system

### 367 4.3. Experimental results and discussion

368 The experimental results of the combined system were obtained and compared with  
369 the theoretical results. Moreover, the pre-desalination system was tested separately to

370 gauge the performance of the desalination process.

371 **4.3.1. Experimental results of the refrigeration and pre-desalination system**

372 The ammonia flux of the desalination branch is maintained by controlling the valve;  
 373 subsequently, the substep desalination experiment of the desalination branch is  
 374 performed. The primary and detailed experimental results are shown in Table 5. Table  
 375 6 shows the average data of the substep experiment and the desalination rate at each  
 376 desalination stage. A set of selected experimental data for the whole combined system  
 377 is shown in Table 7.

378 **Table 5** Experimental results of the pre-desalination system

Experiment serial number	1	2	3	4	5	6	7	8	9	10	11	12	13	14
Initial seawater	100	100	100	100	100	100	100	100	100	100	100	100	100	100
Flux (L/h)	100	100	100	100	100	100	100	100	100	100	100	100	100	100
Stage 1														
Salinity (ppt)	35.0	35.0	34.8	34.7	35.0	34.9	35.0	35.0	35.0	34.9	35.0	34.8	35.0	35.0
Seawater flux after														
evaporator I (L/h)	40.5	37.0	34.8	36.3	33.0	34.1	35.8	32.6	38.1	41.9	35.6	32.4	39.5	34.2
Salinity (ppt)	22.7	21.7	19.5	21.2	20.1	23.0	24.8	20.5	22.0	21.9	20.8	21.4	20.7	23.8
Stage 2														
Seawater flux before														
evaporator II (L/h)	40.0	37.0	35.0	36.0	33.0	34.0	36.0	32.5	38.0	42.0	35.5	32.5	39.5	34.0
Salinity (ppt)	23.0	22.0	19.7	21.0	20.0	23.0	25.0	20.5	22.0	22.0	21.0	21.5	20.7	24.0
Pre-desalinated														
seawater flux(L/h)	22.3	19.5	21.2	21.8	21.0	19.6	21.1	20.5	20.5	21.3	20.8	20.5	22.2	20.8
Salinity (ppt)	8.7	9.8	9.5	8.5	8.4	8.3	11.5	10.0	9.0	9.0	9.3	8.8	10.5	9.4

379

380 **Table 6** Desalination rate of each desalination stage

	Seawater position	Flux (L/h)	Average Salinity (ppt)	Desalination rate (%)
Stage 1	Initial seawater	100	35.0	38.0
	Seawater after evaporator I	36.1	21.7	
Stage 2	Seawater before evaporator II	36.1	21.8	57.3
	Pre-desalinated seawater	20.9	9.3	

381 The experimental results demonstrate that the salinity of seawater was reduced to

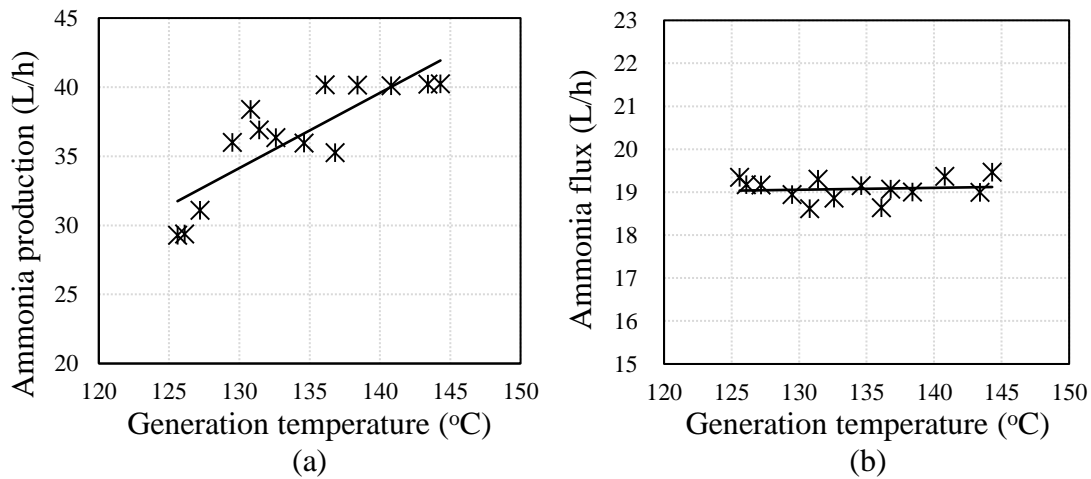
382 the range of 19.5 ppt to 24.8 ppt after the first-stage freezing desalination, and reduced  
 383 to the range of 8.3 ppt to 11.5 ppt after the second stage. On average, the salinity of the  
 384 seawater was reduced to 21.7 ppt and the desalination rate was 38.0% in the first-stage  
 385 desalination process. The salinity of the pre-desalinated seawater was reduced to 9.3  
 386 ppt and the desalination rate was 57.3% in the second-stage desalination process. The  
 387 desalination rate in the second stage was higher than that in the first stage, which is  
 388 beneficial to the crystallisation of pure water.

389 **Table 7** Experimental performance of the refrigeration and pre-desalination system

Ammonia system												
Before condenser °C	After condenser °C	Total flux L/h	Generation pressure MPa	Absorption pressure MPa	Cold storage branch				Desalination branch			
					Evaporation temperature °C	Return gas temperature °C	Flux L/h	Cold storage °C	Evaporation temperature °C	Return gas temperature °C	Flux of evaporator I L/h	Flux of evaporator II L/h
					76.4	31.5	38.8	0.96	0.03	-21.7	-14.4	20.7
Cooling water system						Rich ammonia solution		Weak ammonia solution				
Before absorber °C	After absorber °C	Flux of absorber m <sup>3</sup> /h	After dephlegmator °C	Flux of dephlegmator m <sup>3</sup> /h	After condenser °C	After absorber °C	After heat exchanger °C	After generator °C	After heat exchanger °C			
23.5	25.5	12.0	57.8	0.24	27.2	27.5	121.4	130.8	43.5			
Heating water of thawing tank					Seawater of the desalination branch							
Before thawing tank I °C	After thawing tank I °C	Before thawing tank II °C	After thawing tank II °C	Flux L/h	Seawater flux before evaporator I L/h	Seaice flux after evaporator I L/h	Seaice salinity after evaporator I ppt	Seawater flux before evaporator II L/h	Seaice flux after evaporator II L/h	Seaice salinity after evaporator II ppt		
					100.0	36.3	21.2	36.0	21.8	8.5		

390 In this list of selected experimental data for the whole combined system, we found  
 391 that the total ammonia production was 38.8 L/h. The ammonia flux of the cold storage  
 392 branch was 20.7 L/h and that of the desalination branch was 19.6 L/h. The sum of the  
 393 two branches was 40.3 L/h, which is slightly different than that of the total ammonia  
 394 production. This difference is caused by measurement errors. Under these ammonia

395 fluxes, the temperature of the cold storage reached  $-8.4\text{ }^{\circ}\text{C}$ , while the evaporation  
 396 temperature reached approximately  $-21\text{ }^{\circ}\text{C}$ . With this evaporation temperature, the  
 397 salinity of the pre-desalinated seawater was reduced to 8.5 ppt through the two stages  
 398 of the freezing desalination process. The production rate of the pre-desalinated seawater  
 399 was 21.8 L/h. If the desalination scale or the refrigeration requirement for cold storage  
 400 is increased, the temperature of the inlet exhaust gas can be further increased to improve  
 401 the refrigeration output for the whole system.



402

403

404

405

406

407

408

409

410

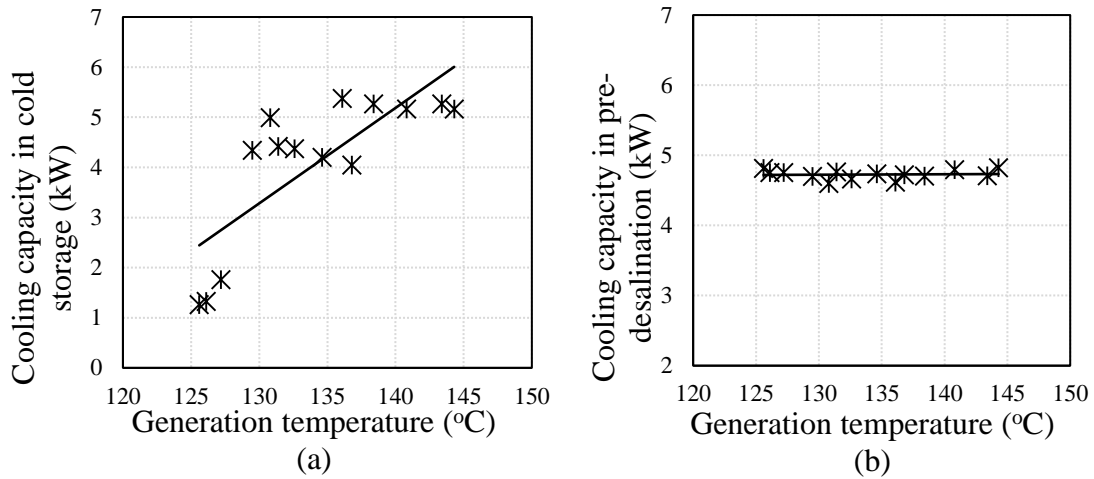
411

Fig.6 Ammonia output: (a) Total ammonia production;

(b) Ammonia flux of pre-desalination branch

Figure 6(a) shows the relationship between the total ammonia production and the generation temperature. The result shows that, with the continuous improvement in the generation temperature, the total production of ammonia increases. When the generation temperature reached  $140\text{ }^{\circ}\text{C}$ , the total ammonia production increased to 40 L/h. Figure 6(b) illustrates the relationship between the ammonia flux of the desalination branch and the generation temperature. We found that through the control of the valve, the ammonia flux was maintained between 18 L/h and 20 L/h.

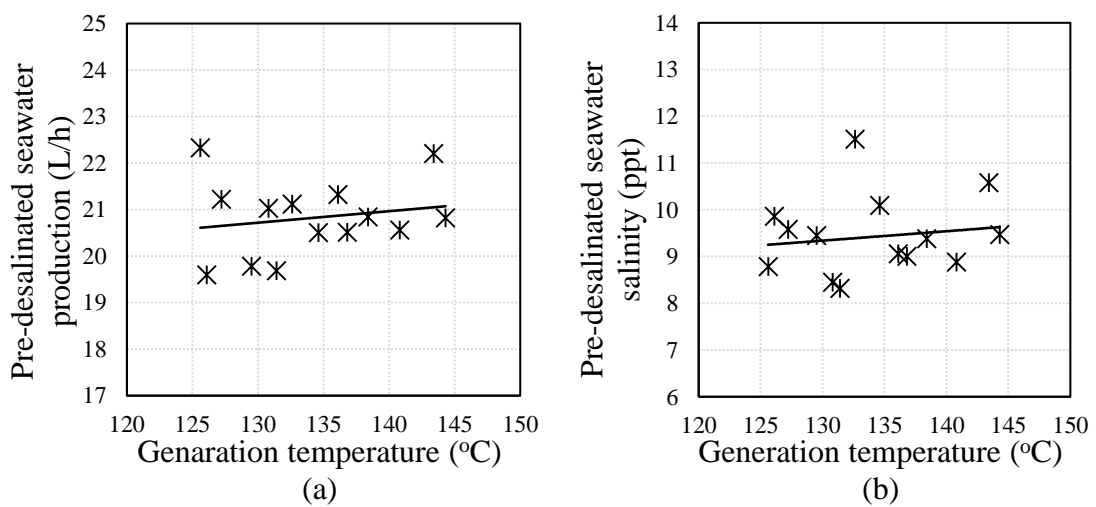




412 Fig.7 Cooling capacity of two branches: (a) Cold storage branch;

413 (b) Pre-desalination branch

414 Figure 7 depicts the cooling capacity performances of the two branches. The cooling  
 415 capacity of the cold storage branch ranged from 1.2 kW to 5.2 kW, as shown in Fig.7(a).  
 416 The cooling capacity of the pre-desalination branch was maintained at approximately  
 417 4.7 kW, as shown in Fig. 7(b). As indicated in the figure, a rising trend in the cooling  
 418 capacity occurs in the cold storage branch with the continuous improvement of the  
 419 generation temperature, while the cooling capacity in the pre-desalinated branch is  
 420 maintained at a constant.  
 421



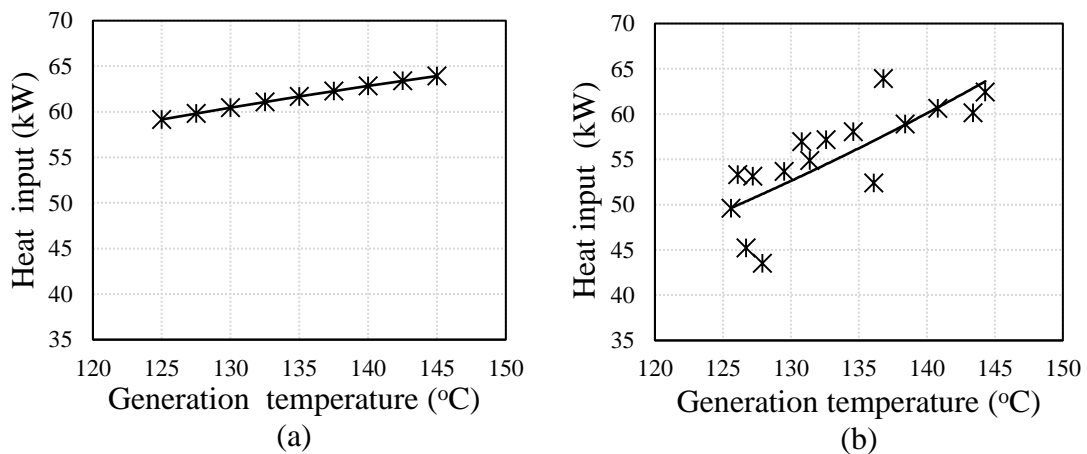
422 Fig.8 Pre-desalinated seawater output: (a) Production; (b) Salinity

423

424 Figure 8(a) illustrates the relationship between the production of pre-desalinated  
 425 seawater and the generation temperature. The result shows that the pre-desalinated  
 426 seawater production was primarily maintained between 20 L/h and 22 L/h. Figure 8(b)  
 427 shows the performance of the pre-desalinated seawater salinity. We found that the pre-  
 428 desalinated seawater salinity was primarily maintained below 10 ppt, thus achieving  
 429 the expected freezing-assisted desalination target.

430 **4.3.2. Comparison of system performances between experimental and theoretical**  
 431 **results**

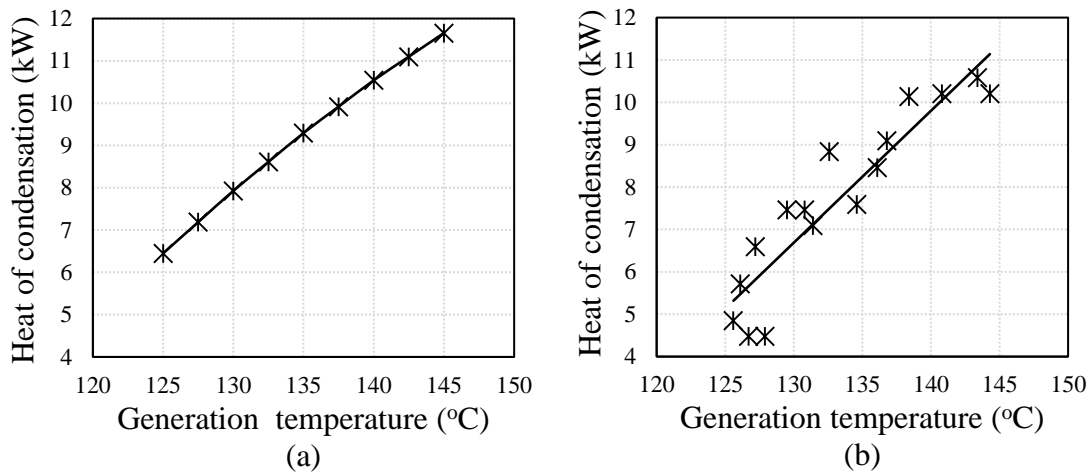
432 The generator heat input, condenser heat output, absorber heat output, refrigeration  
 433 output, and system COP were experimentally obtained and compared with the  
 434 theoretical results.



435  
 436 Fig.9 Comparison of generator heat input: (a) Theoretical generator heat input;  
 437 (b) Experimental generator heat input

438 The results of the theoretical generator heat input obtained according to Eq.(8) and  
 439 Eq.(9) are shown in Fig. 9(a). The flue gas composition at the generator inlet and outlet

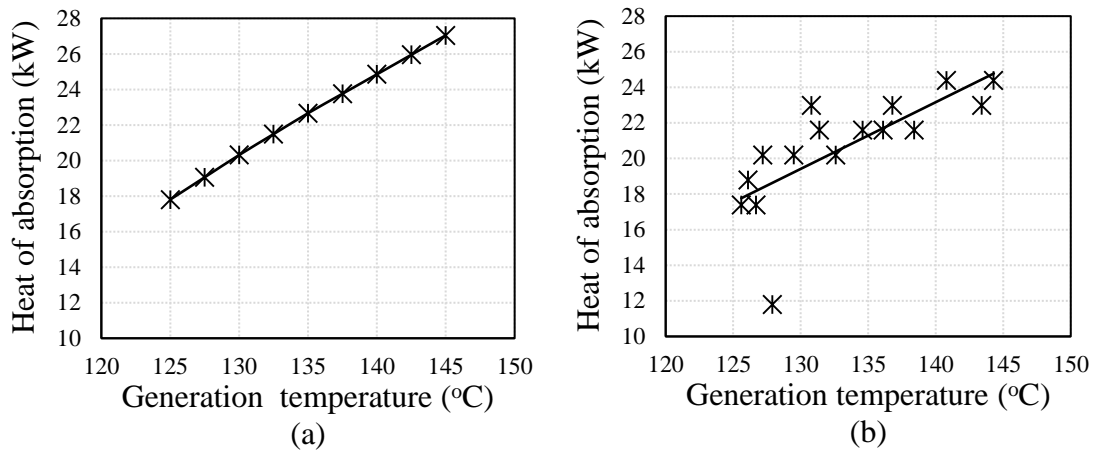
440 was detected by a flue gas analyser, and the results of the experimental generator heat  
 441 input obtained according to the flue gas composition[33] are shown in Fig. 9(b). The  
 442 experimental and theoretical generator heat inputs were compared. The theoretical heat  
 443 input ranged from 58 kW to 64 kW, and the experimental heat input ranged from 50  
 444 kW to 64 kW; meanwhile, the generation temperature ranged from 125 °C to 145 °C.  
 445 The experimental generator heat input showed a faster increasing trend than the  
 446 theoretical generator heat input. The error of the experimental and theoretical curves  
 447 was approximately 8%.



448  
 449 Fig.10 Comparison of condenser heat output: (a) Theoretical condenser heat output;  
 450 (b) Experimental condenser heat output

451 The comparison between the theoretical and experimental results of the system heat  
 452 of condensation is shown in Fig. 10. The theoretical heat of condensation obtained  
 453 according to Eq. (10) and Eq. (11) ranged from 6 kW to 12 kW, and the experimental  
 454 heat of condensation ranged from 5 kW to 11 kW. Meanwhile, the generation  
 455 temperature ranged from 125 °C to 145 °C. In the same generation temperature range,  
 456 the experimental heat of condensation was lower than the theoretical heat of

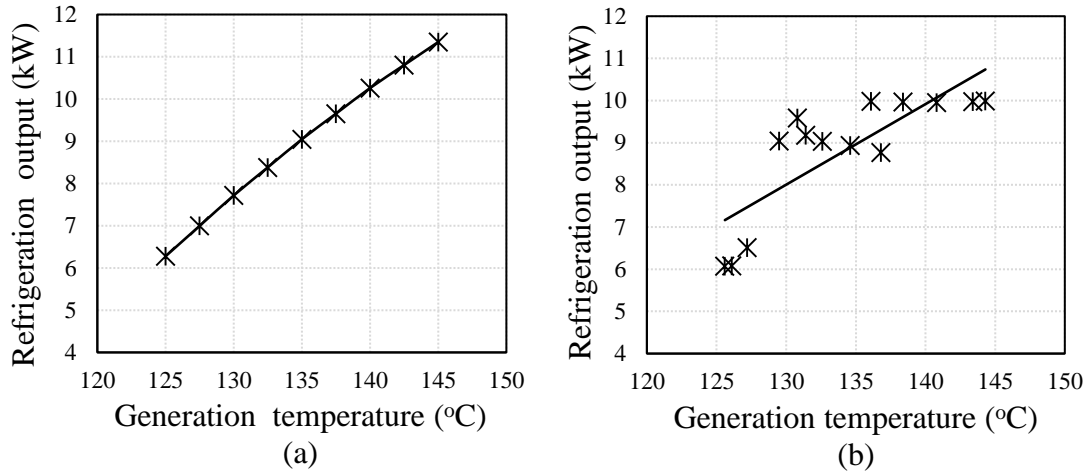
457 condensation by approximately 10%. Because the unit operation time was during the  
 458 winter, the indoor air temperature was low, i.e. approximately 10 °C. Considering the  
 459 heat loss caused by the heat exchange between the refrigerant and air, the actual heat of  
 460 condensation would be slightly greater than the measured data.



461  
 462 Fig.11 Comparison of absorber heat output: (a) Theoretical absorber heat output; (b)

463 Experimental absorber heat output

464 The comparison between the theoretical and experimental results of the system heat  
 465 of absorption is shown in Fig. 11. The theoretical heat of absorption obtained according  
 466 to Eq. (12) and Eq. (13) ranged from 18 kW to 27 kW, and the experimental heat of  
 467 absorption ranged from 17 kW to 25 kW, while the generation temperature ranged from  
 468 125 °C to 145 °C. In the same generation temperature range, the experimental absorber  
 469 heat output was lower than the theoretical absorber heat output by approximately 7%.  
 470 Considering the heat exchange between the refrigerant and the winter air, the actual  
 471 heat of absorption would be slightly greater than the measured data.



472

473 Fig.12 Comparison of refrigeration output: (a) Theoretical refrigeration output; (b)

474

Experimental refrigeration output

475

476

477

478

479

480

481

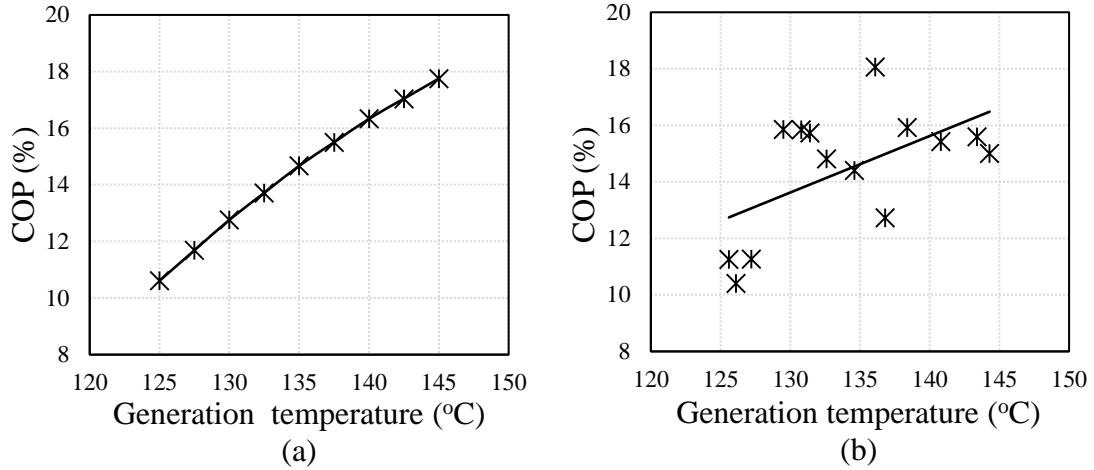
482

483

484

485

The comparison between the theoretical and experimental results of the system refrigeration output is shown in Fig.12. The theoretical refrigeration output obtained according to Eq. (14) and Eq. (15) ranged from 6.3 kW to 11.3 kW, and the experimental refrigeration output ranged from 6.1 kW to 9.9 kW. Meanwhile, the generation temperature ranged from 125 °C to 145 °C. We found that the refrigeration output, which is a function of the ammonia liquid balance in the system, exhibited a large gradient when the generation temperature was close to 130 °C. When the generation temperature is close to 130 °C, the total ammonia production of the system is increased, and the ammonia liquid stored in the ammonia liquid tank is sufficient. At this time, the ammonia liquid flow at the outlet of the ammonia liquid tank is increase by adjusting the valve, which leads to the cooling capacity exhibiting a large gradient.



486

487

Fig.13 Comparison of COP: (a) Theoretical COP; (b) Experimental COP

488

The comparison between the theoretical and experimental results of the system COP

489

is shown in Fig. 13. The theoretical COP ranged from 10.5% to 18%, and the

490

experimental COP ranged from 10% to 16%. Meanwhile, the generation temperature

491

ranged from 125 °C to 145 °C. In the same generation temperature range, the

492

experimental COP was lower than the theoretical COP by approximately 7%.

493

## 5. Economic analysis

494

The cost of the general RO desalination device primarily includes two parts: the

495

electricity consumption cost and the membrane replacement cost.

496

The total cost is defined as

497

$$F_{total} = F_{elec} + F_{mem} + F_{else}. \quad (36)$$

498

The electricity consumption cost is defined as

499

$$F_{elec} = F_u M_w M_t, \quad (37)$$

500

where  $F_u$  is the unit electricity consumption cost (yuan/kWh),  $M_w$  is the

501

operation power of the RO device (kW), and  $M_t$  is the operation time of the RO device

502 (h).

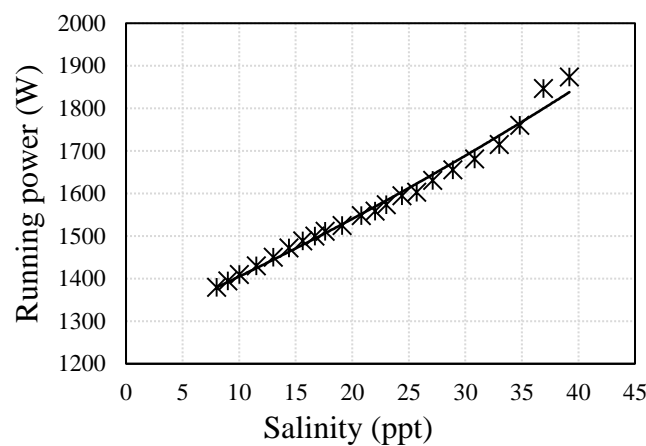
503 The membrane replacement cost is defined as[34]

$$504 \quad F_{mem} = 0.723M_oM_p^{-1}M_L^{-1}, \quad (38)$$

505 where  $M_o$  is the component cost (yuan/piece),  $M_p$  is the component output (L/d),  
506 and  $M_L$  is the component lifetime (year).

507  $F_{else}$  includes the labour cost, spare parts cost, and reagent cost. For small-scale  
508 RO desalination devices,  $F_{else}$  is low and even negligible.

509 According to Eq. (37), the electricity consumption cost primarily depends on the  
510 operating power and operating time of the RO device. The operating power of the RO  
511 device is associated with the salinity of the influent seawater. Figure 14 shows the  
512 relationship between the operating power of the RO device and the salinity of influent  
513 seawater. The experiment device is a small-scale RO device (Model: YB-SWRO-500L)  
514 with a high-pressure pump. We found that reducing the salinity of influent seawater  
515 significantly reduced the operating power of the RO device.



516

517 Fig.14 Relationship between the operating power of the small-scale RO device

518

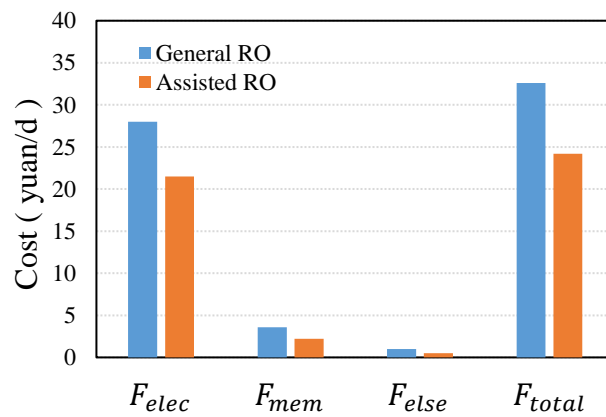
and the salinity of influent seawater

519

Under the same membrane lifetime, the total desalination cost of the brackish water

520 was lower than the total desalination cost of the initial seawater. Furthermore, under the  
 521 same fresh water output, the membrane lifetime increased with the decrease in the  
 522 seawater salinity. Generally, a long lifetime has little impact on the total cost; however,  
 523 if mis-operation or a change in influent water causes the component lifetime to shorten,  
 524 it can significantly affect the total cost.

525 The average salinity of the pre-desalinated seawater was 9.3 ppt after the two-stage  
 526 freezing-assisted desalination process. For the small-scale RO device of YB-SWRO-  
 527 500L, we assumed that the operating time was 12 h/day. The total RO cost of the pre-  
 528 desalinated seawater was compared with the total RO cost of the initial seawater with  
 529 an average salinity of 35 ppt, and the result is shown in Fig. 15. Finally, the total cost  
 530 of freezing-assisted RO was calculated to be less than the total cost of general RO by  
 531 approximately 26%.



532  
 533  
 534 Fig.15 General RO and assisted RO cost comparison

535 **6. Conclusion**

536 We herein introduced an absorption refrigeration and two-stage freezing-assisted  
 537 desalination system for recovering waste heat from marine diesel engine flue gas. The



538 refrigeration produced by this system could be used for low-temperature cold storage  
539 and seawater freezing-assisted desalination. A mathematical model and solution  
540 procedure of the system were developed to predict its performance, and an experimental  
541 platform was established to evaluate its performance. During the experiment, the total  
542 ammonia production was continuously increased by the continuous increase in the  
543 influent flue gas temperature. The ammonia flux of the desalination branch was  
544 maintained by controlling the valve, while the ammonia flux of the cold storage branch  
545 was continuously increased. Consequently, stable production of pre-desalinated  
546 seawater and a low-temperature cold storage were obtained. Based on our analysis,  
547 the following conclusions were drawn.

- 548 • With the concentration of the ammonia-water rich solution at 0.28 kg/kg and  
549 the generation temperature increasing from 125 °C to 145 °C, the system COP  
550 could be increased from 10% to 16%. The total refrigeration output varied from  
551 6.1 kW to 9.9 kW and the cooling capacity of the cold storage sub-branch was  
552 increased from 1.2 kW to 5.2 kW, and the cooling capacity of the pre-  
553 desalination branch was maintained at approximately 4.7 kW.
- 554 • With the pre-desalination process, the production of pre-desalinated seawater  
555 was primarily maintained between 20 L/h and 22 L/h when the flux of the initial  
556 seawater was 100 L/h. Furthermore, the salinity of the pre-desalinated seawater  
557 was reduced to below 10 ppt from an initial value of 35 ppt.
- 558 • The generator heat input, condenser heat output, absorber heat output,  
559 refrigeration output, and system COP increased as the generation temperature

560 increased. Additionally, the production and salinity of the pre-desalinated  
561 seawater remained at the same level as the generation temperature varied.

- 562 • The cost of RO seawater desalination could be reduced by 26% through  
563 seawater pre-desalination.

## 564 **Acknowledgements**

565 The authors would like to acknowledge the financial support from National Natural  
566 Science Foundation of China (51706214), Key Basic Research of Shandong Provincial  
567 Natural Science Foundation (ZR2017ZA0203) and Central University of basic  
568 scientific research business fees special of China (201713034).

## 569 **References**

- 570 [1]. Deng, B., Q. Tang and M. Li, Study on the steam-assisted Brayton air cycle for exhaust heat  
571 recovery of internal combustion engine. *Applied Thermal Engineering*, 2017. 125.
- 572 [2]. Fu, J., et al., Energy and exergy analysis on gasoline engine based on mapping characteristics  
573 experiment. *Applied Energy*, 2013. 102(2): p. 622-630.
- 574 [3]. Yüksel, F. and M.A. Ceviz, Thermal balance of a four stroke SI engine operating on hydrogen as a  
575 supplementary fuel. *Energy*, 2003. 28(11): p. 1069-1080.
- 576 [4]. Taymaz, I., An experimental study of energy balance in low heat rejection diesel engine. *Energy*,  
577 2006. 31(2 - 3): p. 364-371.
- 578 [5]. Galindo, J., et al., Further analysis of a compression-expansion machine for a Brayton Waste Heat  
579 Recovery cycle on an IC engine. *Applied Thermal Engineering*, 2017.
- 580 [6]. Gopal, N.K., et al., Thermodynamic Analysis of a Diesel Engine Integrated with a PCM Based  
581 Energy Storage System. *International Journal of Thermodynamics*, 2010. 13(1).
- 582 [7]. Kyriakidis, F., et al., Modeling and optimization of integrated exhaust gas recirculation and multi-  
583 stage waste heat recovery in marine engines. *Energy Conversion & Management*, 2017. 151: p. 286-295.
- 584 [8]. Kim, S.L., et al., Evaluation of automotive waste heat recovery for various driving modes. *Energy*,  
585 2016. 106: p. 579-589.
- 586 [9]. Chen, Y., W. Han and H. Jin, Thermodynamic performance optimization of the absorption-  
587 generation process in an absorption refrigeration cycle. *Energy Conversion & Management*, 2016. 126:  
588 p. 290-301.
- 589 [10]. Salek, F., A.N. Moghaddam and M.M. Naserian, Thermodynamic analysis of diesel engine coupled

590 with ORC and absorption refrigeration cycle. *Energy Conversion & Management*, 2017. 140: p. 240-246.

591 [11]. Maryami, R. and A.A. Dehghan, An exergy based comparative study between LiBr/water  
592 absorption refrigeration systems from half effect to triple effect. *Applied Thermal Engineering*, 2017.  
593 124(9): p. 103-123.

594 [12]. Cerezo, J., et al., Experimental study of an ammonia - water bubble absorber using a plate heat  
595 exchanger for absorption refrigeration machines. *Applied Thermal Engineering*, 2009. 29(5): p. 1005-  
596 1011.

597 [13]. Arshi Banu, P.S. and N.M. Sudharsan, Review of water based vapour absorption cooling systems  
598 using thermodynamic analysis. *Renewable & Sustainable Energy Reviews*, 2018. 82.

599 [14]. Ibrahim, N.I., F.A. Al-Sulaiman and F.N. Ani, Performance characteristics of a solar driven lithium  
600 bromide-water absorption chiller integrated with absorption energy storage. *Energy Conversion &*  
601 *Management*, 2017. 150: p. 188-200.

602 [15]. Moreno, D., et al., Absorption refrigeration cycles based on ionic liquids: Refrigerant/absorbent  
603 selection by thermodynamic and process analysis. *Applied Energy*, 2018. 213: p. 179-194.

604 [16]. Wu, X., S. Xu and M. Jiang, Development of bubble absorption refrigeration technology: A review.  
605 *Renewable & Sustainable Energy Reviews*, 2018. 82.

606 [17]. Alelyani, S.M., et al., Techno-economic analysis of combined ammonia-water absorption  
607 refrigeration and desalination. *Energy Conversion & Management*, 2017. 143: p. 493-504.

608 [18]. Sun, J., L. Fu and S. Zhang, A review of working fluids of absorption cycles. *Renewable &*  
609 *Sustainable Energy Reviews*, 2012. 16(4): p. 1899-1906.

610 [19]. Srihirin, P., S. Aphornratana and S. Chungpaibulpatana, A review of absorption refrigeration  
611 technologies. *Renewable & Sustainable Energy Reviews*, 2000. 5(4): p. 343-372.

612 [20]. Li, Y. and R. Hu, Exergy-analysis based comparative study of absorption refrigeration and electric  
613 compression refrigeration in CCHP systems. *Applied Thermal Engineering*, 2016. 93: p. 1228-1237.

614 [21]. Kang, Z., et al., Research Status of Ice-storage Air-conditioning System. *Procedia Engineering*,  
615 2017. 205: p. 1741-1747.

616 [22]. Song, X., et al., Study of economic feasibility of a compound cool thermal storage system  
617 combining chilled water storage and ice storage. *Applied Thermal Engineering*, 2018.

618 [23]. Liu, S., et al., Impacts on the solidification of water on plate surface for cold energy storage using  
619 ice slurry. *Applied Energy*, 2017.

620 [24]. Tamasauskas, J., et al., Development and validation of a solar-assisted heat pump using ice slurry  
621 as a latent storage material. *Solar Energy*, 2012. 21(6): p. 837-846.

622 [25]. Xie, C., et al., A direct contact type ice generator for seawater freezing desalination using LNG cold  
623 energy. *Desalination*, 2017.

624 [26]. Jayakody, H., R. Al-Dadah and S. Mahmoud, Computational fluid dynamics investigation on  
625 indirect contact freeze desalination. *Desalination*, 2017. 420: p. 21-33.

626 [27]. Mandri, Y., et al., Parametric study of the sweating step in the seawater desalination process by  
627 indirect freezing. *Desalination*, 2011. 269(1-3): p. 142-147.

628 [28]. Shapiro, J., Freezing-Out, a Safe Technique for Concentration of Dilute Solutions. *Science*, 1961.  
629 133(3470): p. 2063.

630 [29]. Rich, A., et al., Sea water desalination by dynamic layer melt crystallization: Parametric study of  
631 the freezing and sweating steps. *Journal of Crystal Growth*, 2012. 342(1): p. 110-116.

632 [30]. Luo, C.S., W.W. Chen and W.F. Han, Experimental study on factors affecting the quality of ice  
633 crystal during the freezing concentration for the brackish water. *Desalination*, 2010. 260(1 - 3): p. 231-

634 238.

635 [31]. Williams, P.M., et al., Technology for freeze concentration in the desalination industry.  
636 Desalination, 2015. 356(3): p. 314-327.

637 [32]. Ziegler, B. and C. Trepp, Equation of state for ammonia-water mixtures. International Journal of  
638 Refrigeration, 1984. 7(2): p. 101-106.

639 [33]. Du, S., R.Z. Wang and X. Chen, Development and experimental study of an ammonia water  
640 absorption refrigeration prototype driven by diesel engine exhaust heat. Energy, 2017. 130.

641 [34]. C.J. Gao and G.L. Ruan, Seawater desalination technology and engineering. Chemical Industry  
642 Press, 2016: p. 296.

643